

## Fast and Reliable Detection of Significant Solitons in Signals with Large Time-Bandwidth Products

Koster, Pascal de; Wahls, Sander

**DOI**

[10.1109/JLT.2023.3285434](https://doi.org/10.1109/JLT.2023.3285434)

**Publication date**

2023

**Document Version**

Final published version

**Published in**

Journal of Lightwave Technology

**Citation (APA)**

Koster, P. D., & Wahls, S. (2023). Fast and Reliable Detection of Significant Solitons in Signals with Large Time-Bandwidth Products. *Journal of Lightwave Technology*, 41(20), 6586-6598.  
<https://doi.org/10.1109/JLT.2023.3285434>

**Important note**

To cite this publication, please use the final published version (if applicable).  
Please check the document version above.

**Copyright**

Other than for strictly personal use, it is not permitted to download, forward or distribute the text or part of it, without the consent of the author(s) and/or copyright holder(s), unless the work is under an open content license such as Creative Commons.

**Takedown policy**

Please contact us and provide details if you believe this document breaches copyrights.  
We will remove access to the work immediately and investigate your claim.

***Green Open Access added to TU Delft Institutional Repository***

***'You share, we take care!' - Taverne project***

**<https://www.openaccess.nl/en/you-share-we-take-care>**

Otherwise as indicated in the copyright section: the publisher is the copyright holder of this work and the author uses the Dutch legislation to make this work public.

# Fast and Reliable Detection of Significant Solitons in Signals With Large Time-Bandwidth Products

Pascal de Koster  and Sander Wahls , *Senior Member, IEEE*

**Abstract**—We present a fast method to calculate the significantly large solitonic components of signals with large time-bandwidth products governed by the nonlinear Schrödinger equation, for which the computation typically becomes prohibitively expensive and/or numerically unstable. We partition the full signal in both frequency and time to obtain short signals with a constant number of samples, independent of the size of the full signal. The solitons within each short signal are computed using a conventional nonlinear Fourier transform (NFT) algorithm. The partitioning in general leads to spurious solitons not present in the full signal. We therefore design an acceptance scheme that removes spurious solitons. The remaining solitons are attributed to the full signal. Solitons that are too wide to fit into the short signals cannot be detected by this approach, but since wide solitons must be of low amplitude, the significant solitons will be found. This approach only requires  $\mathcal{O}(N)$  floating point operations, with  $N$  the number of signal samples. It can furthermore be applied to signals with large time-bandwidth products for which conventional NFT algorithms become unreliable or even fail. When applying our proposed method to a signal of 15,000 samples, the significant solitonic components were computed 14 times faster than when considering the whole signal, for which the conventional algorithm furthermore provided wrong results. We found that time-partitioning yields accurate results, while frequency-partitioning causes a small loss in accuracy. Combined frequency-time partitioning leads to the fastest computation, but also suffers from the same loss in accuracy as with frequency-partitioning. As time-partitioning yields a significant speed-up at nearly no loss in accuracy, we regard this as the method of choice in most practical scenarios.

**Index Terms**—Nonlinear Schrödinger equation, solitons, nonlinear Fourier transform, forward scattering transform.

## I. INTRODUCTION

THE nonlinear Schrödinger equation (NLSE) describes wave propagation in optical fibers [1]. The lossless NLSE is known for the existence of so-called solitons, which are localized particle-like waves [2], [3]. Even though individual solitons have a distinctive hyperbolic secant shape for the NLSE, they often cannot be determined by visual inspection of a wave packet because nonlinear interactions with other signal components temporarily change their form. In such cases, the nonlinear

Fourier transform (NFT) is nevertheless able to detect them [4], [5]. Due to their stability, solitons have found many applications in fiber optics, such as fiber-optical communication [6], [7], [8], [9], [10], [11], [12], [13], [14], [15], [16], fiber parameter estimation [17], [18], the analysis of laser radiation [19], [20], [21], [22], optical resonators [23], [24] and optical combs [25]. It is well known that the number of hidden solitons in a rectangular pulse grows with both its amplitude and duration, see e.g., [6]. This suggests that especially long and/or high power signals are typically rich in solitons. Accordingly, conventional orthogonal frequency division multiplexing (OFDM) and Nyquist-shaped communication signals with long durations and/or powers have surprisingly been observed to contain large numbers of hidden solitons [17], [26].

The numerical computation of the NFT is however a nontrivial problem due its nonlinear nature. Even though many different algorithms to compute the discrete part of the NFT that corresponds to solitons have been proposed in the literature (e.g., search methods [27], [28], [29], [30], [31], matrix methods [28], [30], [32], subdivision methods [29], [33], machine learning methods [34], phase tracking [35] and all-pass filter synthesis [36]), a wave packet with 32 solitons is still considered a challenging example [35]. For more complicated signals, the numerical algorithms often become computationally expensive and/or unreliable when using standard double precision floating point arithmetic. The efficient detection of the potentially hidden solitons in signals with large time-bandwidth products would be directly relevant for example in fiber parameter identification [17], [18], soliton-based communication systems [7], [14], [15], [16], [37], [38], [39], analysis of optical soliton gases [40], [41], optical rogue wave analysis [42], as well as in areas outside fiber optics (e.g., ocean waves [43], [44], [45]).

Since solitons are localized in both the physical and the frequency domain, it should however be possible to accurately calculate the significantly large solitons using only a limited part of the full signal. This would result in a faster and more reliable calculation. Several previous studies have indeed already observed that solitons are not influenced by other signal components that are sufficiently separated in the time or frequency domain [44], [46], [47]. If we thus take a sufficiently large frequency-time window, the significant solitons in the center of the window are expected not to be influenced by the solitons outside the window.

In this article, we propose a novel method based on these findings to quickly calculate the significant solitons within a

Manuscript received 27 February 2023; revised 11 May 2023 and 26 May 2023; accepted 5 June 2023. Date of publication 13 June 2023; date of current version 16 October 2023. (Corresponding author: Pascal de Koster.)

The authors are with the Delft Center for System and Control, Delft University of Technology, 2628 CD Delft, Netherlands (e-mail: p.b.j.dekoster@tudelft.nl; s.wahls@tudelft.nl).

Color versions of one or more figures in this article are available at <https://doi.org/10.1109/JLT.2023.3285434>.

Digital Object Identifier 10.1109/JLT.2023.3285434

signal. Our idea is to partition the full signal into shorter signals, and/or band-pass filtered signals. The center frequencies of the band-pass filtered signals are temporarily shifted to zero such that they can be captured with less samples. The signals with less samples are then evaluated separately. We define rectangular frequency-time windows of fixed bandwidth  $\Delta\Omega^{\text{window}}$  and duration  $\Delta T^{\text{window}}$ , and cover the full rectangular frequency-time domain of the original signal with such windows. The windows are allowed to overlap. The signal content in each window can then be captured with only  $M \leq N$  samples, where  $N$  is the number of samples of the full signal (proportional to the time-bandwidth product of the full signal), and  $M$  the number of samples of the windowed signal (proportional to the smaller time-bandwidth product of the frequency-time windows). The computation time for a single windowed signal will thus only depend on  $M$  and the chosen NFT method, but does not scale with the full signal length  $N$ . As we require  $\mathcal{O}(\frac{N}{M})$  windows to cover the entire frequency-time domain, the computation of the significant eigenvalues in the discrete spectrum can thus be performed with only  $\mathcal{O}(N)$  floating point operations (FLOPs). The proposed method does not suffer from numerical reliability issues that normally arise for signals with large time-bandwidth products due to the nonlinear nature of the NFT. Spurious solitons, which can occur as a result of the partitioning, are avoided by rejecting solitons whose support is not sufficiently contained within the window. The impact of the partitioning on the estimated soliton parameters is controlled by taking sufficiently large sub-domains of the signal. This allows us to quickly and reliably find the significant solitons of the full signal. Here, solitons are considered significant if their amplitudes are above a threshold that only depends on the chosen window sizes.

Our main contributions are as follows. We formalize the above ideas of partitioning the signal and calculating the eigenvalues associated to the significant solitons from small frequency-time windows. We derive a heuristic for the minimal required window size to be able to capture all significant solitons. By letting the windows overlap, we can ensure that all significant eigenvalues are captured, although some eigenvalues may be doubly captured. We then introduce an acceptance scheme, to keep only the most reliable version of eigenvalues that were captured in multiple windows due to their overlap, and to reject unreliable or spurious eigenvalues. Finally, we demonstrate the accuracy and speed of this frequency- and time-windowing method on several signals with large time-bandwidth products.

This article is organized as follows. Section II will recapitulate the nonlinear Fourier transform to define the eigenvalues associated with the solitonic components. Section III will define the window size based on the required support to capture the expected soliton content and describes an algorithm to reject spurious or inaccurate eigenvalues. Section IV summarizes the final algorithm. Section V tests the described frequency- and time-windowing algorithm on signals with large time-bandwidth products. Finally, Section VI concludes the article.

## II. SOLITONS, THE NONLINEAR FOURIER TRANSFORM, AND SOLITON LOCATION

We consider the focusing nonlinear Schrödinger equation (NLSE) for signals with vanishing tails [1],

$$q_z = iq_{tt} + 2i|q|^2q, \quad q \xrightarrow{t \rightarrow \pm\infty} 0 \text{ sufficiently fast,} \quad (1)$$

with  $q(t, z)$  the complex signal amplitude and  $i$  the imaginary unit. Subscripts denote partial derivatives. We consider the normalized and unitless NLSE, but for the sake of clarity we will refer to  $t$  as time and  $z$  as position, which is often the case in fiber optics [1]. The normalization procedure itself depends on the application, but can be found in the corresponding literature. For fiber optics, see e.g. [6, Eq. 3] or [17, Eq. 5].

The focusing NLSE has soliton solutions, which are particle-like waves that retain their shape even after interacting with other solitons or dispersive waves. The defocusing NLSE, which differs from (1) by a sign in front of the nonlinear term, in contrast has no soliton solutions. A pure 1-soliton solution of the NLSE may be associated with a complex eigenvalue  $\lambda_k = \xi_k + i\eta_k$  ( $\xi_k \in \mathbb{R}$ ,  $\eta_k > 0$ ), where  $k$  is an index that is used later for signals containing multiple solitons. We refer to  $\lambda_k$  as an eigenvalue because it arises as such from a spectral problem, as explained in the next section. The 1-soliton solution is given by [5]

$$q_k(t, z; \lambda_k, t_k^0, \psi_k^0) = \overbrace{2\eta_k \operatorname{sech} \left( 2\eta_k \left( t - t_k^0 - \underbrace{\left( -4\xi_k \right)}_{c_k} z \right) \right)}^{\text{envelope}} \times \underbrace{\exp \left( -2i\xi_k(t - t_k^0) - \psi_k^0 - 4i(\xi_k^2 - \eta_k^2)z \right)}_{\text{carrier}}, \quad (2)$$

in which  $t_k^0$  and  $\psi_k^0$  are, respectively, the time and phase offset of the soliton at  $z = 0$ . The envelope wave speed is  $c_k = -4\xi_k$ . For the rest of this article we will assume  $z = 0$ , as we are not interested in the propagation of solitons. We note some important properties of the 1-soliton.

- The envelope shape is only determined by the eigenvalue height  $\eta_k = \Im(\lambda_k)$ : the soliton amplitude scales linearly with  $\eta_k$ , but the soliton also becomes narrower, as illustrated in Fig. 1.
- The carrier is only determined by the real part  $\xi_k = \Re(\lambda_k)$ . The linear center frequency of this soliton is given by  $\omega_k = -2\xi_k$ . Shifting the real part of the eigenvalue by  $\Delta\xi$  thus causes a linear frequency shift of  $\Delta\omega = -\Delta\xi/2$  and vice versa.
- The energy of the 1-soliton is given by

$$E_k = \int_{-\infty}^{\infty} |q_k(t, z; \lambda_k)|^2 dt = 4\eta_k, \quad (3)$$

so the highest eigenvalues (i.e., with the largest imaginary part  $\eta_k$ ) contain the most energy.

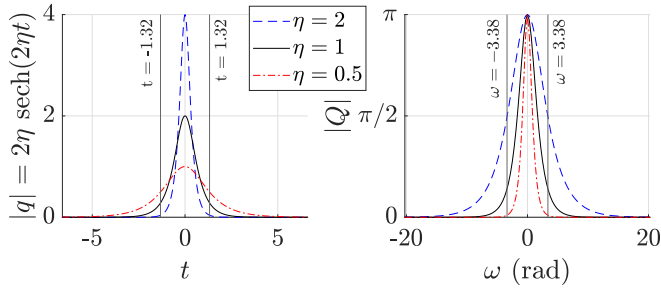


Fig. 1. Envelope of three solitons with different  $\eta$  in the time- and frequency-domain, and the 99%-energy support of the unit soliton with  $\eta = 1$  (vertical lines).

If we consider an arbitrary signal with  $K$  solitonic components with different speeds (i.e.,  $\xi_k \neq \xi_j$  if  $k \neq j$ ), the solitons will eventually separate, and evolve into a train of  $K$  1-solitons [48], [49]:

$$q(t, z) \approx \sum_{k=1}^K q_k(t, z; \lambda_k, t_k^\pm, \psi_k^\pm), \text{ as } z \rightarrow \pm\infty. \quad (4)$$

When considering an arbitrary signal, this separation will probably not have happened for practically relevant values of  $z$ . Instead, the solitons may be packed close together, and interact with one another as well as with the dispersive part of the signal. In this case, the solitons typically cannot be distinguished visually. To identify which solitons are present, the nonlinear Fourier transform is often employed.

#### A. The Nonlinear Fourier Transform

The soliton content of a signal  $q(t)$  governed by the NLSE can be determined by the NFT. The NFT is defined through the Zakharov-Shabat scattering problem [4],

$$\frac{\partial}{\partial t} \begin{bmatrix} \phi^{(1)}(t, \lambda) \\ \phi^{(2)}(t, \lambda) \end{bmatrix} = \begin{bmatrix} -i\lambda & q(t) \\ -q^*(t) & i\lambda \end{bmatrix} \begin{bmatrix} \phi^{(1)}(t, \lambda) \\ \phi^{(2)}(t, \lambda) \end{bmatrix}, \quad (5a)$$

$$\text{s.t.} \begin{bmatrix} e^{-i\lambda t} \\ 0 \end{bmatrix} \xrightarrow{t \rightarrow -\infty} \begin{bmatrix} \phi^{(1)}(t, \lambda) \\ \phi^{(2)}(t, \lambda) \end{bmatrix} \xrightarrow{t \rightarrow +\infty} \begin{bmatrix} a(\lambda)e^{-i\lambda t} \\ b(\lambda)e^{+i\lambda t} \end{bmatrix}, \quad (5b)$$

in which  $\phi(t, \lambda)$  is the vector eigenfunction corresponding to the complex spectral parameter  $\lambda = \xi + i\eta$ , and  $a(\lambda)$  and  $b(\lambda)$  are the scattering coefficients that characterize the behavior at the right boundary conditions in (5b). The naming convention of ‘eigenfunction’, ‘spectral parameter’ and ‘eigenvalue’ are because the Zakharov-Shabat scattering problem may be rewritten as  $L\phi = \lambda\phi$ , with  $L$  a linear operator. Each  $\lambda_k$  related to a solitonic component in (4) turns out to be an eigenvalue of  $L$ , with eigenfunction  $\phi_k$ .

The full NFT of  $q(t)$  consists of a continuous spectrum and a discrete spectrum. We define the continuous spectrum over the real axis,  $\Lambda^c := \{b(\xi) : \xi \in \mathbb{R}\}$ . This spectrum corresponds to the dispersive wave content of the signal. The continuous spectrum is mentioned here for completeness, but we are not further interested in it throughout this article.

We define the discrete (solitonic) spectrum using the zeros of  $a(\lambda)$  in the upper half plane,  $\Lambda^d := \{(\lambda_k, b(\lambda_k)) : a(\lambda_k) = 0, \Im(\lambda_k) > 0\}$ , where  $b_k = b(\lambda_k)$  denotes the solution of (5) at  $\lambda_k$ . Methods for the computation of  $a(\lambda)$  and  $b(\lambda)$  can e.g. be found in [27], [28], [30], [50]. Such methods can be utilized to find the  $\lambda_k$  in various ways, as was pointed out in the introduction. The computation of  $b_k$  is known to yield numerical issues without special precautions, but we overcome this by computing  $b_k$  with the NLSE-version of the adapted bidirectional algorithm from [51]. The eigenvalues  $\lambda_k = \xi_k + i\eta_k$  correspond to those in the previously mentioned 1-soliton solutions. The eigenvalue  $\lambda_k$  defines the shape and speed of the soliton, while the  $b$ -coefficient  $b_k = b(\lambda_k)$  provides information about the soliton location and phase [5]. As a signal propagates according to the normalized NLSE in (1), all eigenvalues remain constant, and the  $b$ -coefficients evolve in a simple manner:

$$b(\lambda; z) = b(\lambda; 0)e^{4i\lambda^2 z} \Rightarrow |b_k(z)| = |b_k(0)|e^{-8\xi\eta z}. \quad (6)$$

#### B. Soliton Location

At the start of this section, we noted that every 1-soliton is localized at  $t_k^0$  (at  $z = 0$ ), where the peak of its envelope is located. For the further analysis in this article, we assume that hidden solitons in a general signal are also localized around some soliton location  $t_k$ , similar to a 1-soliton. If we take a sufficiently large section of the full signal around that soliton location, it should be possible to detect the associated soliton accurately by computing the NFT of that section. The soliton location can usually only be observed visually in the far field, where all solitons have separated and the dispersive part becomes negligible. Therefore, we define a novel soliton location  $t_k$  for the near field when the solitons have not separated yet, suitable for the purpose in this article. The idea for  $t_k$  is to find an initial soliton location from  $b_k$ , assuming that the soliton is isolated. Then we refine that initial soliton location by taking all soliton interactions into account.

First, we assign each soliton a ‘1-soliton location’  $\hat{t}_k$ , which corresponds with the location of the soliton derived from  $b_k$  if the signal had been a 1-soliton with eigenvalue  $\lambda_k$  as given in (2) [48], [49, Eq. 1.7],

$$\hat{t}_k = \frac{\ln |b_k|}{2\eta_k}. \quad (7)$$

Next, we refine the 1-soliton locations by taking all the pairwise soliton interactions into account. Let two solitons be represented by  $(\lambda_1, b_1)$  and  $(\lambda_2, b_2)$ . Fig. 2(a) compares the corresponding individual 1-solitons, and the 2-soliton with this discrete spectrum (i.e., a signal with exactly two eigenvalues, and zero continuous spectrum). Clearly, the locations of the peaks have shifted away from each other in the 2-soliton, despite the fact that the same  $b$ -coefficients were used. The result of the soliton interaction is that the solitons are pushed apart: the left one further to the left, and the right one further to the right.

To approximate the size of this shift, we consider the total shift between the soliton peaks as one overtakes the other, as is illustrated in Fig. 2(b) and (c). When the interaction is fully

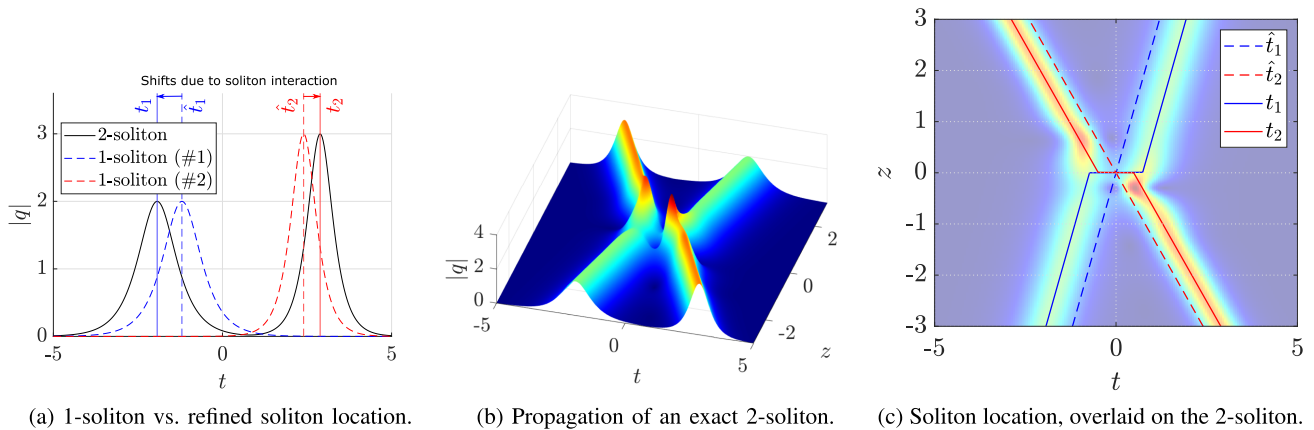


Fig. 2. Illustration of the soliton location, by comparing a 2-soliton with two 1-solitons with the same spectrum. Spectral data of the two solitons are  $(\lambda_1 = -0.1 + 1i, b_1 = \exp(2i))$  and  $(\lambda_2 = 0.2 + 1.5i, b_2 = \exp(0))$  at  $z = 0$ . **Left**: the 2-soliton at  $z = -3$  compared to the two 1-solitons with the same spectral data  $(\lambda_k, b_k)$ . The corresponding 1-soliton locations  $\hat{t}_k$  and soliton locations  $t_k$  are indicated, as well as the shift due to the soliton interaction. **Middle**: the propagation of the 2-soliton. Soliton 1 overtakes solitons 2 at  $z = 0$ . **Right**: the 1-soliton locations and final soliton locations, overlaid on the propagating 2-soliton. Note the jump in  $t_1$  and  $t_2$  as result of the overtaking at  $z = 0$ .

completed, the total time shift for soliton  $k$  as result of the interaction with soliton  $j$  is given by [49, Eq. 1.18]:

$$\Delta t_{k,j} = \frac{1}{\eta_k} \left| \ln \left| \frac{\lambda_k - \lambda_j}{\lambda_k - \lambda_j^*} \right| \right|. \quad (8)$$

For the soliton location, we assume that the interaction is instantaneous, and add (resp. subtract) half the total time shift to (from) the 1-soliton location if the soliton  $k$  is right (left) of soliton  $j$ . We add half the time shift, as the interaction is symmetric, and when the right- and left-most solitons switch place (as if one overtook the other), the result would indeed be the full time shift. Fig. 2(c) shows the result of the soliton location for a 2-soliton before, during and after the interaction. Indeed the soliton locations corresponds very well to the peak locations, even close to the interaction.

For a multi-soliton signal, it is well known that the total time shift is simply the summation of all pair-wise time shifts [48]. We thus define the refined soliton location as the 1-soliton location, compensated for every soliton-pair interaction:

$$t_k = \hat{t}_k + \sum_{j=1, j \neq k}^K \text{sign}(\hat{t}_k - \hat{t}_j) \frac{1}{2\eta_k} \left| \ln \left| \frac{\lambda_k - \lambda_j}{\lambda_k - \lambda_j^*} \right| \right|. \quad (9)$$

Note that we disregard the interaction with the continuous spectrum. This choice is deliberate, as it is hard to determine which dispersive components are ‘left’ or ‘right’ of the soliton, while it is only significant when much of the energy is in the continuous spectrum. We obtained good results without it, although we only considered signals with most of the energy in the discrete spectrum.

It has been observed empirically that various pulse shaping methods commonly employed for fiber-optical communications can be dominated by solitons at practically relevant transmit powers [17], [26]. For a specific class of NFT-based fiber-optic transmitters, it has even been proven that without using solitons, the signal power must approach zero as the signal duration

increases [52]. Ignoring the continuous spectrum in the soliton location is therefore often a reasonable approximation.

### III. PARTITIONING THE FREQUENCY-TIME DOMAIN INTO WINDOWS, AND ACCEPTING EIGENVALUES

In this section, we define heuristics to choose the frequency-time window size to capture the significant solitons accurately. We will find, consistently with (2), that the significant (i.e., higher amplitude and  $\eta_k$ , respectively) solitons occupy a broad bandwidth but short duration, while solitons with lower eigenvalues occupy longer durations, but shorter bandwidths. To ensure that the windows can capture all of the significant solitons, we first estimate the mean eigenvalue height using the mean energy density, and adjust the window size accordingly. Next, we allow the windows to overlap to ensure that all higher solitons are captured. Finally, we filter out unreliable and/or doubly-detected solitons with an eigenvalue acceptance scheme.

#### A. Estimation of the Mean Eigenvalue Height

We wish to choose a window size such that all significant solitons can be captured. To do so, we start by estimating a ‘mean’ eigenvalue height  $\eta^{\text{mean}}$  of the solitons in the signal, as the eigenvalue height will be the decisive factor for the required bandwidth and duration of the windows. To estimate the mean eigenvalue height, we define a mean energy density  $\rho^{\text{mean}}$  over the considered frequency-time domain, and then estimate the mean eigenvalue height of the signal by comparing the mean energy density of the signal to the mean energy density of a 1-soliton.

First, we define the mean energy density  $\rho^{\text{mean}}$  of a 1-soliton as the total energy, divided by the time-bandwidth product that captures most of the energy. Let the 99%-energy ( $p = 0.99$ ) bandwidth (resp. duration) be defined as the smallest bandwidth (resp. duration) required to capture a fraction  $p$  of the total signal energy. For a 1-soliton  $q_k$  with  $\xi_k = 0$  and  $t_k = 0$  as shown in

Fig. 1, the support bandwidth and duration are

$$\int_{-\frac{\Delta T_k}{2}}^{\frac{\Delta T_k}{2}} |q_k(t)|^2 dt = \underbrace{pE_k}_{0.99(4\eta_k)} \Rightarrow \Delta T_k = \frac{2.64}{\eta_k}, \quad (10a)$$

$$\frac{1}{2\pi} \int_{-\frac{\Delta\Omega_k}{2}}^{\frac{\Delta\Omega_k}{2}} |Q_k(\omega)|^2 d\omega = pE_k \Rightarrow \Delta\Omega_k = 6.75\eta_k, \quad (10b)$$

where  $Q_k(\omega) = \int_{-\infty}^{\infty} q_k(t)e^{-i\omega t} dt$ , i.e., the Fourier transform of  $q_k(t)$ . The time-bandwidth product  $\Delta\Omega_k\Delta T_k = 17.82$  rad of a 1-soliton does not depend on  $\eta_k$  because they are related to each other through time- and amplitude scalings, which leave the time-bandwidth product invariant. We then define the mean energy density of a 1-soliton with eigenvalue height  $\eta_k$  as its total energy ( $E_k = 4\eta_k$ ), divided by its time-bandwidth product:

$$\rho_k^{\text{mean}} = \frac{E_k}{\Delta T_k \Delta\Omega_k} = \frac{4\eta_k}{17.82} = 0.224\eta_k. \quad (11)$$

Next, we calculate the mean energy density of the signal too as the total energy divided by its 99%-energy bandwidth  $\Delta\Omega$  and 99%-energy duration  $\Delta T$ . Finally we estimate that the ‘mean’ soliton has the same mean energy density as the signal  $\rho_q^{\text{mean}}$ ,

$$\rho_q^{\text{mean}} = 0.224\eta^{\text{mean}} \Rightarrow \eta^{\text{mean}} = \frac{\rho_q^{\text{mean}}}{0.224} = \frac{E_q}{0.244\Delta\Omega\Delta T}, \quad (12)$$

with  $\eta^{\text{mean}}$  the ‘mean’ eigenvalue height. Note that the mean eigenvalue height only roughly indicates a center for the final eigenvalue cloud. It does not correspond with the actual mean height, as low eigenvalues usually appear more frequently than high ones.

### B. Choosing the Window Frequency-Time Size

After establishing the estimated mean eigenvalue height, we will choose the frequency-time window sufficiently large to capture all eigenvalues which have  $\eta_k$  around the estimated eigenvalue height. We will first define a significant frequency-time support of a soliton with eigenvalue  $\lambda$ , and then design the frequency-time window large enough such that it can contain the significant support of all significant solitons of interest. We finally create the window size based on the expected mean eigenvalue height defined in (12), and the height range of eigenvalues that we want to capture.

We assume that a soliton with the mean eigenvalue height  $\eta^{\text{mean}}$  occupies a rectangular frequency-time support of  $\Delta\Omega \times \Delta T$ , with  $\Delta\Omega = 6.74\eta^{\text{mean}}$  and  $\Delta T = 2.64/\eta^{\text{mean}}$ , centered around its soliton location  $t_k$  and center frequency ( $\omega_k = -2\xi_k$ ). To capture higher eigenvalues we require a larger bandwidth  $\Delta\Omega$ , and for lower eigenvalues a longer duration  $\Delta T$ . To capture a wide range of solitons, we chose the window bandwidth as  $c_\Omega = 16$  times the mean-eigenvalue bandwidth, and the window duration as  $c_T = 4$  times the mean-eigenvalue duration:

$$\Delta\Omega^{\text{window}} \times \Delta T^{\text{window}} = \underbrace{c_\Omega}_{=16} (6.74\eta^{\text{mean}}) \times \underbrace{c_T}_{=4} (2.64/\eta^{\text{mean}}). \quad (13)$$

We made the bandwidth 16 times larger to ensure that all high eigenvalues are captured. We made the duration only four times larger because this mainly allowed us to capture more low eigenvalues, in which we are less interested. This window size gave us accurate results for signals with approximate uniform energy distribution of the occupied frequency-time domain, but of course the window size may be tailored to specific applications. When only time-windowing is desired, simply set the frequency-window size equal to the full occupied bandwidth  $\Delta\Omega^{\text{window}} = \infty$ , and vice versa for only frequency-windowing.

### C. Dividing the Domain and Window Overlap

After deciding on the window size, we will cover the entire occupied frequency-time domain with windows of this size. The most straightforward method would be to use as few windows as possible while still covering the entire domain. However, we could then miss several high eigenvalues with soliton location  $t_k$  or center frequency  $\omega_k$  close to the window edges. Part of the soliton support would then fall outside the window, and the detected eigenvalue could be significantly distorted as a result.

To ensure that all higher eigenvalues are captured well by at least one window, we let all neighboring windows overlap for a fraction of at least  $0 \leq R < 1$  for both frequency- and time-windowing. After creating the equispaced windows with this minimum overlap fraction, the actual time overlap fraction  $R_T \geq R$  and frequency overlap fraction  $R_\Omega \geq R$  are often slightly larger because the number of windows is an integer number. In the worst-case scenario for time-windowing (resp. frequency-windowing), a soliton has its  $t_k$  (resp.  $\omega_k$ ) exactly in the middle of the overlapping region, such that the largest soliton support fully contained in either window is  $R_T\Delta T^{\text{window}}$  (resp.  $R_\Omega\Delta\Omega^{\text{window}}$ ) units. Following (10) and (13), the lowest  $\eta_k$  thus captured within this time support and the highest  $\eta_k$  captured within this frequency support are

$$\eta_k \in [\eta^{\min}, \eta^{\max}] = \left[ \frac{1}{Rc_T} \eta^{\text{mean}}, Rc_\Omega \eta^{\text{mean}} \right]. \quad (14)$$

Note that when using only time-windowing (resp. frequency-windowing), only the lower (resp. upper) limit is relevant. Lower values of  $R$  will narrow down the range of solitons in (14) we can capture reliably. Choosing higher values of  $R$  causes windows to overlap more, requiring more windows and thus more computation time. A well-balanced overlap fraction is thus around  $R = 0.5$ . Instead of choosing even higher  $R > 0.5$  and thus increasing the number of required windows,  $c_\Omega$  or  $c_T$  (i.e., the window size) can also be increased to capture a wider range, which is often computationally faster.

The full domain is thus covered as follows:

- 1) Choose a window size  $\Delta\Omega^{\text{window}} \times \Delta T^{\text{window}}$  and overlap fraction  $0 \leq R < 1$ .
- 2) Cover the full frequency domain  $\Omega$  with equispaced frequency sections of size  $\Delta\Omega^{\text{window}}$  such that consecutive sections overlap for a fraction of at least  $R$ . This results in  $N_\Omega$  frequency sections  $\Omega^{(n)}$ ,  $1 \leq n \leq N_\Omega$ . If  $\Delta\Omega^{\text{window}} > \Delta\Omega$ , set  $\Delta\Omega^{\text{window}} = \infty$ , and  $N_\Omega = 1$ .

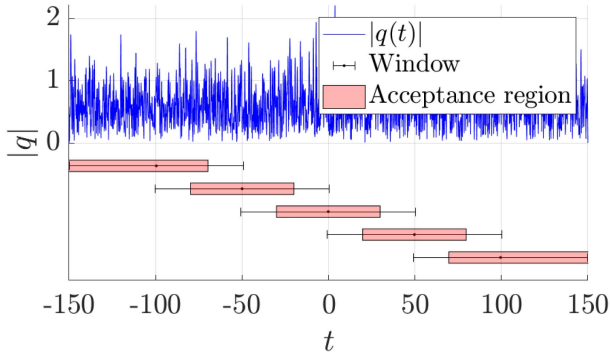


Fig. 3. Exemplary signal of duration  $\Delta T = 300$ , with its associated time windows (shown below the signal) using  $R = 0.5$  (neighboring windows overlap at least 50%), and the corresponding acceptance regions using  $\varepsilon = 0.05$ . For  $\varepsilon = 0$ , the acceptance regions would not overlap, and would exactly partition the time domain.

- 3) Do the same for the time domain  $T$  with equispaced sections of size  $\Delta T^{\text{window}}$ , resulting in  $M_T$  time sections  $T^{(m)}$ ,  $1 \leq m \leq M_T$ .
- 4) Define  $N_\Omega \times M_T$  frequency-time windows  $\Omega^{(n)} \times T^{(m)}$  as the cross product of the frequency section and time sections.

This process is illustrated on the left in Fig. 4 with slight offsets to improve visibility.

We note here that we only cover the 99%-energy bandwidth and 99%-energy duration of the full signal  $\Delta\Omega \times \Delta T$ , and thus cut away parts of the signal. We do so to be able to assign any signal a finite bandwidth and duration to avoid wasting computation time analyzing any slowly decaying tails of the signal (either in frequency or time domain), which generally do not contain high solitons. However,  $\Omega$  and  $T$  may also be set manually if clear bounds for the signal are known.

#### D. Creating Windowed Signals

After defining the frequency-time windows, we extract a short signal for each window. First, we apply an ideal band-pass filter to the full signal to remove all frequency content outside of  $\Omega^{(n)}$  by calculating the Fourier transform of the full signal, and setting all frequencies components outside  $\Omega^{(n)}$  to zero. Next, we temporarily shift the center frequency  $\omega_n$  (middle of  $\Omega^{(n)}$ ) to zero for the filtered signal,  $q(t) \rightarrow q(t)e^{-i\omega_n t}$  (i.e.,  $Q(\omega) \rightarrow Q(\omega - \omega_n)$ ), such that the filtered frequency content can be captured without aliasing with much fewer samples than before the center shift, namely using sampling time  $\Delta t < \frac{2\pi}{\Delta\Omega^{\text{window}}}$ . The center frequency is added back later to the detected eigenvalues, where we will use that linear frequency shifting a signal results in a linear shift in the real part  $\xi_k$  of each eigenvalue:  $q(t) \rightarrow q(t)e^{-i\omega_n t} \Rightarrow \xi_k \rightarrow \xi_k + \omega_n/2$  [6, p. 4319, D6, frequency shift property].

After frequency-windowing, the filtered signal is time-windowed by only keeping those samples within the time-window  $T^{(m)}$ , resulting in a short signal containing the signal content within the frequency-time window  $\Omega^{(n)} \times T^{(m)}$ . We used rectangular filters/time-windows in our implementation as

the impact of general linear filters and time-windows on the nonlinear Fourier spectrum is not well-understood.

#### E. Eigenvalue Acceptance

After all the frequency- and time-windowed signals have been created, the eigenvalues of each windowed signal are computed using the NFT and the center frequency is added back to the real part of the eigenvalues again,  $\lambda_k \rightarrow \lambda_k - \omega_n/2$ . The eigenvalues from the windowed signal are estimations for the eigenvalues of the full signal. However, many of the eigenvalues from the full signal will have been affected by the windowing process, and we wish to only keep the eigenvalues that are also present in the full signal. We therefore introduce an acceptance criterion for the eigenvalues of the windowed signal.

The idea for the eigenvalue acceptance is that the soliton support (see (10)) should lie entirely within the window. The required time-support of an eigenvalue grows with  $1/\eta_k$ , so the lowest eigenvalues will require a broader time-support than the window duration. We should therefore discard the too-low eigenvalues by default. Similarly, the highest eigenvalues require a large frequency-support. We set the acceptance height range for the detected eigenvalue height equal to the earlier defined eigenvalue capture region from (14), and reject all eigenvalues outside this height range. The frequency-windows should be chosen sparsely, so that it is nearly guaranteed that the highest eigenvalues are captured. An additional rough measure for the highest eigenvalue present (based on the 1-soliton in (2)) is the maximum absolute wave height  $\max_k \eta_k \propto |q|/2$ . Choosing the frequency-window size such that  $\eta^{\text{max}} \gg \max_t |q(t)|/2$  ensured that the highest solitons were captured for our data.

After rejecting all eigenvalues below the acceptance height range, it may still occur that several of the remaining eigenvalues are too close to the window edge, such that their significant support still lies partially outside the considered window. These eigenvalues should thus be rejected. To do so, we first determine the soliton location  $t_k$  from (9) using the  $(\lambda_k, b_k)$  of every soliton above the acceptance height of the considered window. Next, we assign each window an associated acceptance region as defined below, which corresponds to the window minus a narrow strip near the window edges. The idea is that we only keep those eigenvalues from the windowed signal that also have their frequency-time location  $(\omega_k = -\xi_k/2, t_k)$  within the acceptance region of that window.

We initially define the acceptance region  $\Omega_+^{(n)} \times T_+^{(m)}$  of a window as the part of the full frequency-time domain closer to the center of the window than to any other window center, as shown in Fig. 4. The result is that all overlapping regions are exactly split into half and divided equally over the two overlapping windows. For the overlap fraction  $R_\Omega$  (resp.  $R_T$ ), the initial frequency (resp. time) acceptance region  $\Omega_+^{(n)} = [\Omega_{+,l}^{(n)}, \Omega_{+,r}^{(n)}]$  (resp.  $T_+^{(m)} = [T_{+,l}^{(m)}, T_{+,r}^{(m)}]$ ) is thus a fraction  $R_\Omega/2$  (resp.  $R_T/2$ ) smaller on both sides than the frequency-window  $[\Omega_l^{(n)}, \Omega_r^{(n)}]$  (resp. time-window  $[T_l^{(m)}, T_r^{(m)}]$ ). Here, the subscript  $l$  is short for ‘left’ and  $r$  is short for ‘right’. We thus get  $[\Omega_{+,l}^{(n)}, \Omega_{+,r}^{(n)}] =$

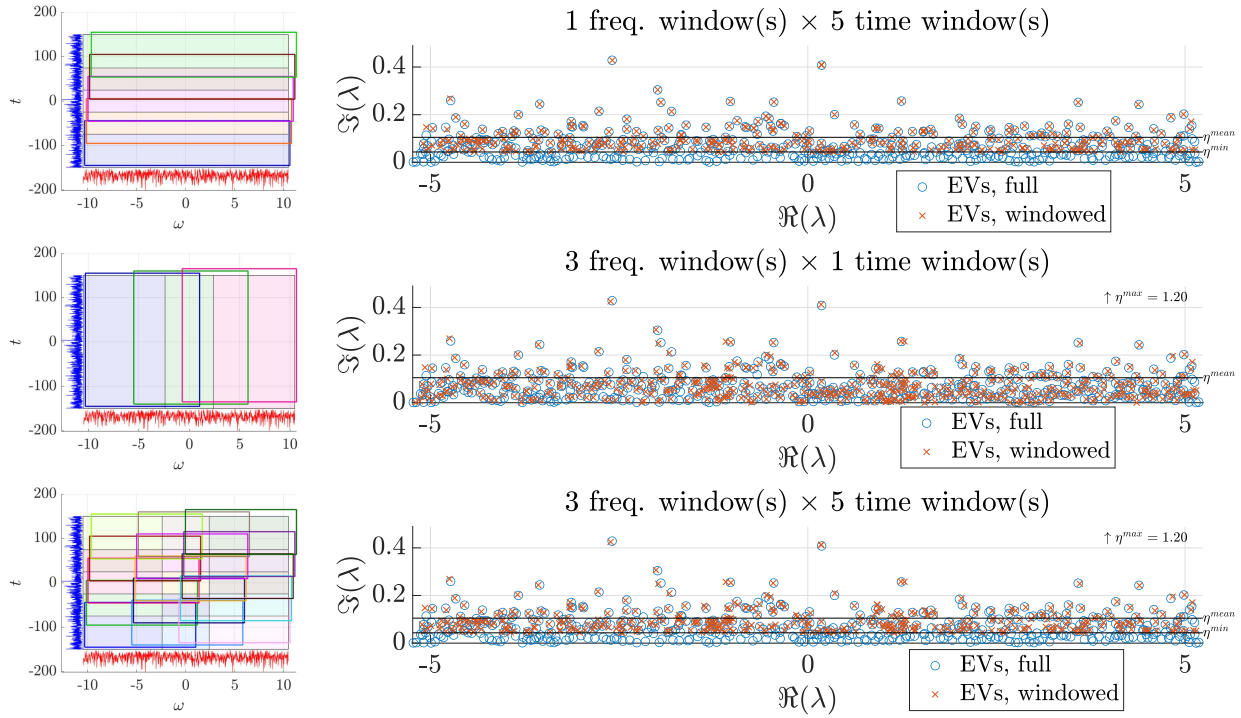


Fig. 4. Comparison between the eigenvalues found by the NFT of a full 3000 sample signal and the corresponding windowed signals using Algorithm 1 and Algorithm 2. Three cases were considered for windowing: only time-windowing (top), only frequency-windowing (middle), and combined frequency- and time-windowing (bottom). The left column shows the used windows (windows are slightly offset for visibility). The bandwidth limited noise signal  $|q(t)|$  is shown in blue at the left of the domain and  $|Q(\omega)|$  below in red for illustration purposes (not to scale). Both  $q(t)$  and  $Q(\omega)$  quickly decay outside the shown domain  $\Omega \times T = [-10.47, 10.47] \text{ rad} \times [-150, 150]$ . The right column shows the full eigenvalue spectrum and the accepted eigenvalues from the windowed signals.

$\left[ \Omega_1^{(n)} + \frac{R_\Omega \Delta \Omega^{\text{window}}}{2}, \Omega_r^{(n)} - \frac{R_\Omega \Delta \Omega^{\text{window}}}{2} \right]$  and  $\left[ T_{+,l}^{(m)}, T_{+,r}^{(m)} \right] = \left[ T_1^{(m)} + \frac{R_T \Delta T^{\text{window}}}{2}, T_r^{(m)} - \frac{R_T \Delta T^{\text{window}}}{2} \right]$ . The left edge of the leftmost frequency-windows and time-windows and right edge of the rightmost windows are not shortened, as those regions are not captured better by any other window. We thus partition the full domain into disjoint acceptance regions, which usually prevents eigenvalues from being detected twice by two neighboring overlapping windows.

However, we found that it may sometimes occur that eigenvalues are entirely missed this way. If a soliton has true soliton frequency-time location  $(\omega_k = -\xi_k/2, t_k)$ , its observed time or frequency location can slightly vary depending on the used window. It may therefore occur that  $t_k$  is on the boundary between two acceptance regions, and that the detected soliton location from the left window is  $t_k + \epsilon$ , and for the right window  $t_k - \epsilon$ . It would then fall outside both windows, and be rejected by both acceptance regions.

To avoid doubly-rejecting eigenvalues that are on the boundaries of the initial acceptance regions, we slightly extend the acceptance regions in both the time and frequency domain by a small fraction  $\epsilon$  of the window size, as illustrated in Fig. 3. The final acceptance regions  $\Omega_+^{(n)} \times T_+^{(m)}$  thus become

$$\left[ \Omega_{+,l}^{(n)}, \Omega_{+,r}^{(n)} \right] = \left[ \Omega_1^{(n)} + \left( \frac{R_\Omega}{2} - \epsilon \right) \Delta \Omega^{\text{window}}, \Omega_r^{(n)} - \left( \frac{R_\Omega}{2} - \epsilon \right) \Delta \Omega^{\text{window}} \right], \quad (15a)$$

$$\left[ T_{+,l}^{(m)}, T_{+,r}^{(m)} \right] = \left[ T_1^{(m)} + \left( \frac{R_T}{2} - \epsilon \right) \Delta T^{\text{window}}, T_r^{(m)} - \left( \frac{R_T}{2} - \epsilon \right) \Delta T^{\text{window}} \right],$$

$$\text{using } \Omega_1^{(1)} = T_1^{(1)} = -\infty, \quad \Omega_r^{(N)} = T_r^{(M)} = +\infty. \quad (15b)$$

A typical value for the acceptance region extension fraction is  $\epsilon = 0.05$ , but should be much smaller than  $R/2$ , else the acceptance region will become larger than the window itself. While the overlap fraction  $R$  itself does not play an active role in the acceptance, we emphasize that it should be chosen sufficiently large to facilitate the capturing of eigenvalues close to window boundaries.

Higher extension fractions  $\epsilon$  increase the chance that all eigenvalues are captured, but also increase the chance that some eigenvalues are captured twice. In choosing the extension fraction, we prioritized ensuring that all high eigenvalues were detected, which caused some eigenvalues to be detected doubly. Higher eigenvalues that are detected twice can often be easily distinguished from the case with two different solitons, as for twice-detected solitons both their  $\lambda_k$  and their  $t_k$  are near-identical. Had those  $\lambda_k$  belonged to two different solitons, then they would have had very different  $t_k$  as it is very hard for the peaks of two different solitons with near-identical  $\lambda_k$  to get close (see (9) and Fig. 2). However, solitons with lower eigenvalues that were captured twice are captured less accurately, and thus it is harder to filter low twice-captured solitons with certainty. The

**Algorithm 1: Creating Frequency-Time Windows.**

Input:

- Signal  $q(t)$  with finite time domain  $D$ .
- Window time-broadening factor  $c_T$  and window frequency-broadening factor  $c_\Omega$  (suggested:  $c_T = 4$ ,  $c_\Omega = 16$ ). Set  $c_T = \infty$  if not time-windowing, and  $c_\Omega = \infty$  if not frequency-windowing.
- Window overlap fraction  $R$  (suggested:  $R = 0.5$ ).
- Acceptance region extension fraction  $\varepsilon$  (suggested:  $\varepsilon = 0.05$ ).

Output:

- A set of frequency-time windows  $\Omega^{(n)} \times T^{(m)}$ , that cover the significant frequency-time domain of  $q(t)$ , and their associated acceptance regions  $\Omega_+^{(n)} \times T_+^{(m)}$ .
- Set  $\Omega_q = [\Omega_l, \Omega_r]$ ,  $T_q = [T_l, T_r]$  as the smallest frequency and time domain containing 99% of the signal energy  $E_q = \int_D |q(t)|^2 dt = \frac{1}{2\pi} \int_{-\infty}^{\infty} |Q(\omega)|^2 d\omega$ ;
- Set  $\Delta\Omega = \Omega_r - \Omega_l$ ,  $\Delta T = T_r - T_l$ ;
- Set  $\eta^{\text{mean}} = \frac{E_q}{0.224\Delta\Omega\Delta T}$ , (see (12));
- Set  $\Delta\Omega^{\text{window}} = \min(c_\Omega 2.64/\eta^{\text{mean}}, \Delta\Omega)$ , and  $\Delta T^{\text{window}} = \min(c_T 6.74\eta^{\text{mean}}, \Delta T)$ , (See (13));
- Set  $N_\Omega = 1 + \lceil \frac{\Delta T - \Delta T^{\text{window}}}{(1-R)\Delta T^{\text{window}}} \rceil$ ,  
 $M_T = 1 + \lceil \frac{\Delta\Omega - \Delta\Omega^{\text{window}}}{(1-R)\Delta\Omega^{\text{window}}} \rceil$ , (the number of required frequency- and time-windows respectively);
- Create  $N_\Omega \times M_T$  frequency-time windows  $\Omega^{(n)} \times T^{(m)}$ ,  $n = 1, \dots, N_\Omega$ ,  $m = 1, \dots, M_T$ , where  $\Omega^{(n)} = [\Omega_n, \Omega_n + \Delta\Omega^{\text{window}}]$  (or  $\Omega^{(1)} = \mathbb{R}$ , if  $N_\Omega = 1$ ), with  $\Omega_n = \Omega_l + (n-1) \frac{\Delta\Omega - \Delta\Omega^{\text{window}}}{\max(N_\Omega - 1, 1)}$ , and  $T^{(m)} = [T_m, T_m + \Delta T^{\text{window}}]$  (or  $T^{(1)} = \mathbb{R}$  if  $M_T = 1$ ), with  $T_m = T_l + (m-1) \frac{\Delta T - \Delta T^{\text{window}}}{\max(M_T - 1, 1)}$ ;
- Set  $R_T = \frac{T_r^{(1)} - T_l^{(2)}}{\Delta T^{\text{window}}}$ ,  $R_\Omega = \frac{\Omega_r^{(1)} - \Omega_l^{(2)}}{\Delta\Omega^{\text{window}}}$  (actual overlap)
- Create  $N_\Omega \times M_T$  acceptance regions  $\Omega_+^{(n)} \times T_+^{(m)} := [\Omega_l^{(n)} + (\frac{R_\Omega}{2} - \varepsilon)\Delta\Omega^{\text{window}}, \Omega_r^{(n)} - (\frac{R_\Omega}{2} - \varepsilon)\Delta\Omega^{\text{window}}] \times [T_l^{(m)} + (\frac{R_T}{2} - \varepsilon)\Delta T^{\text{window}}, T_r^{(m)} - (\frac{R_T}{2} - \varepsilon)\Delta T^{\text{window}}]$ , but with  $\Omega_+^{(1)} = T_+^{(1)} = -\infty$ ,  $\Omega_r^{(N)} = T_r^{(M)} = +\infty$ ;
- Return the windows  $\Omega^{(n)} \times T^{(m)}$  and associated acceptance regions  $\Omega_+^{(n)} \times T_+^{(m)}$ .

focus in this article is on capturing all solitons, so we simply accept it when some solitons are captured twice in this article.

#### IV. SUMMARY OF THE FREQUENCY- AND TIME-WINDOWING NFT ALGORITHM

For completeness, we summarize the steps of the full algorithm. The partitioning of the frequency-time domain into windows is described in Algorithm 1, while the windowing of the full signal and the calculation of the higher eigenvalues from the windowed signals is described in Algorithm 2. For the full estimation of the higher eigenvalues, we first apply

**Algorithm 2: NFT on Windowed Signals.**

Input:

- Signal  $q(t)$ .
- Desired oversampling rate  $s$  (suggested:  $s = 3$ ).
- $N_\Omega \times M_T$  frequency-time windows  $\Omega^{(n)} \times T^{(m)}$  and associated acceptance regions  $\Omega_+^{(n)} \times T_+^{(m)}$ .

Output:

- An approximate set of higher eigenvalues  $\Lambda^{\text{d,high}}$
- Set  $Q(\omega) = \mathcal{F}\{q(t)\}$ ;
- Initialize the set of high eigenvalues  $\Lambda^{\text{d,high}} = \emptyset$ ;
- for**  $n = 1, \dots, N_\Omega$  **do**
  - Set  $Q^{(n)}(\omega) = Q(\omega)$  for  $\omega \in \Omega^{(n)}$ , and  $Q^{(n)}(\omega) = 0$  otherwise (ideal band-pass filtering);
  - Set  $\omega_n = \frac{\Omega_r^{(n)} + \Omega_l^{(n)}}{2}$  (center frequency), and  $\xi^n = -\omega_n/2$  (nonlinear center frequency);
  - Set  $q^{(n)}(t) = \mathcal{F}^{-1}\{Q^{(n)}(\omega - \omega_n)\}$  (center shift, inverse Fourier transform);
  - for**  $m = 1, \dots, M_T$  **do**
    - Set  $q^{n,m}(t) = q^{(n)}(t)$ ,  $q^{n,m}(t \notin T^{(m)}) = 0$ ;
    - Set  $\{\lambda_k, b_k\}_{k=1}^{K^{n,m}} \xleftarrow{\text{Sec. II}} \text{NFT}\{q^{n,m}(t)\}$  (sample  $q^{n,m}(t)$  at  $s$  times the Nyquist frequency, sample time  $\Delta t = \frac{1}{s \min(\Delta\Omega, \Delta\Omega^{\text{window}})}$ );
    - Set  $\{t_k\}_{k=1}^{K^{n,m}} \xleftarrow{\text{Eq. 9}} \{b_k\}_{k=1}^{K^{n,m}}$ ;
    - Accept only the eigenvalues with both  $\eta_k \in [\frac{1}{R_T c_T} \eta^{\text{mean}}, R_\Omega c_\Omega \eta^{\text{mean}}]$  (Eq. 14), and  $(\omega_k = -2\xi_k, t_k)$  within the acceptance region  $\Omega_+^{(n)} \times T_+^{(m)}$ ;
    - Add the accepted eigenvalues  $\lambda_k$  to  $\Lambda^{\text{d,high}}$ ;
- end**
- Return  $\Lambda^{\text{d,high}}$ .

Algorithm 1, followed by Algorithm 2. Algorithm 1 first estimates a representative ‘mean’ soliton height, and chooses the window size accordingly. Next, the occupied domain of the signal is covered with overlapping windows of this size. After defining the windows, Algorithm 2 calculates the higher eigenvalue content in each window. For every window, the full signal is band-pass filtered to the window frequency domain, the center frequency is shifted to zero, and the resulting signal is finally truncated to the window time domain. The eigenvalues of the resulting windowed signal are calculated with the NFT. Eigenvalues are accepted if the eigenvalue height is within the reliable height range, and if the soliton frequency-time location  $(\omega_k, t_k)$  is within the acceptance region. Finally, all accepted eigenvalues are combined for an approximation of the higher eigenvalues of the full signal.

#### V. RESULTS

In this section, we investigate the accuracy and speed for the proposed combined frequency- and time-windowing NFT algorithm, as well as for only time-windowing and only frequency-windowing. First, we test the performance of the algorithm on

a bandwidth-limited random signal, sampled at oversampling rate  $s = 3$ , resulting in 3000 samples. This is the signal with the largest time-bandwidth product that we could produce such that the full NFT could still be reliably calculated with the software library *FNFT* [53] (commit 9756b3, default settings with *4split4B*, with sub-sampling disabled as the considered signals are already sampled close to Nyquist frequency). This method requires  $\mathcal{O}(N^2)$  FLOPs to calculate the discrete spectrum of a signal with  $N$  samples. Second, we investigate the accuracy for a very long signal. For this long signal, the NFT of the full signal can no longer be computed with the mentioned settings of *FNFT*. To validate the accuracy of the windowing NFT, we instead calculate the reference eigenvalues from the full signal by Newton-refining (using the method in [27]) for a dense grid of initial guesses with high precision arithmetic. Third, we quantitatively measure the computation times for the frequency- and/or time-windowing NFT. As combined frequency- and time-windowing uses windows with the smallest time-bandwidth product, this method should yield the largest speed-up.

#### A. Results for a Random 3000-Sample Signal

We first validate the frequency- and time-windowing NFT on a signal with 3000 samples, generated from ideally low-pass filtered, complex, circularly symmetric, zero-mean, white Gaussian noise. This signal has the following properties: time domain  $T = [-150, 150]$ , sample time  $\Delta t = 0.1$ , a maximum bandwidth of  $[-10\pi, +10\pi]$  rad, and occupied bandwidth  $[-10\pi/3, +10\pi/3] = [-10.5, 10.5]$  rad (ideal low-pass filtered, oversampling rate  $s = 3$ ). While *FNFT* in general works well for at this oversampling rate, we found that it occasionally still missed some eigenvalues in both the full NFT and in the windowing NFT. To ensure that we only study the effect of the windowing, we also redid the full and windowing NFTs after upsampling the signal by a factor two using band-limited interpolation, and used those results for Fig. 4. The amplitude of the signal was scaled such that the mean energy density was 0.0224, which corresponds to an expected mean eigenvalue height of  $\eta^{\text{mean}} = 0.1$  according to (12). The corresponding 1-soliton has a frequency-time support of  $0.68 \text{ rad} \times 26$ .

To be able to capture the largest solitons with broad bandwidths, we choose the window bandwidth 16 times the mean eigenvalue bandwidth ( $c_\Omega = 16$ ), and the duration as four times the mean eigenvalue duration ( $c_T = 4$ ). The resulting window size was  $11.3 \text{ rad} \times 101$ . Imposing an overlap fraction of  $R = 0.5$ , we require three frequency-windows  $\Omega^{(n)}$  and five time-windows  $T^{(m)}$ . We thus obtain 15 windows  $\Omega^{(n)} \times T^{(m)}$ , with  $\Omega^{(n)} \in \{[-10.5, 0.8], [-5.4, 5.4], [-0.8, 10.5]\}$ , and  $T^{(m)} \in \{[-150, -49], [-100, 1], [-50, 50], [-1, 100], [49, 150]\}$ . The acceptance region extension fraction was chosen as  $\varepsilon = 0.05$ . The time windows and acceptance regions are also shown in Fig. 3.

We first consider the cases with only time-windowing and only frequency-windowing to observe the individual effects on the detected eigenvalues. Then, we apply both frequency- and time-windowing, which will yield the largest speed-up. The resulting time-windowing, frequency-windowing and combined

frequency- and time-windowing are shown on the left in Fig. 4 (windows are slightly offset for visibility).

1) *Results Using Only Time-Windowing*: In the top row of Fig. 4, the eigenvalues resulting from only time-windowing are shown. We observe that the higher eigenvalues above  $\eta^{\text{mean}}$  correspond very well to the eigenvalues from the full signal. Even the lower eigenvalues between  $\eta^{\text{mean}}$  and  $\eta^{\text{min}}$  seem to be rather accurate.

Upon closer inspection, it turns out that some eigenvalues have been captured doubly by neighboring windows. However, both eigenvalues are so close that they are not visibly distinguishable. As explained, this is due to the acceptance region extension fraction  $\varepsilon = 0.05$ . We also investigated  $\varepsilon = 0$ , and  $\varepsilon = 0.02$ , which respectively resulted in eight and three missing high eigenvalues above  $\eta^{\text{mean}}$ .

We thus find that time-windowing yields very accurate results for the high eigenvalues above  $\eta^{\text{mean}}$ , and fairly good results for the eigenvalues between  $\eta^{\text{min}}$  and  $\eta^{\text{mean}}$ . The acceptance region extension fraction allows a trade-off between increasing the chance to capture all eigenvalues versus capturing some eigenvalues doubly.

2) *Results Using Only Frequency-Windowing*: The windows and detected eigenvalues using only frequency-windowing are shown in the second row of Fig. 4. We observe that the eigenvalues are detected rather accurately, but not as accurately as with time-windowing. The high eigenvalues above  $\eta^{\text{mean}}$  are within 2% of their correct eigenvalue from the full signal. Although frequency-windowing may cut away a part of the frequency support of in particular the highest eigenvalues, this effect seems to be limited. This is likely due to the large frequency-broadening factor  $c_\Omega = 16$ . This hypothesis is supported by the fact that  $\eta^{\text{max}} = 1.20$  is several times larger than the highest eigenvalue. We also observe that a few eigenvalues are also captured twice due to the overlapping acceptance regions. The doubly captured eigenvalues can in several cases be distinguished visually, indicating that the eigenvalues are less accurately captured than for only time-windowing.

Below  $\eta^{\text{mean}}$ , many of the lower eigenvalues seem to be captured with similar accuracy as the higher ones. However, we also observe that many of the lower eigenvalues are missed, but we found that many of these were missed because the oversampling factor  $s$  was too low for the used *FNFT* method, and not due to the frequency windowing itself: upon upsampling the signal using band-limited Fourier interpolation to twice as many samples, many of the missing low eigenvalues were found again. Despite the fact that there is no lower bound  $\eta^{\text{min}}$ , it seems that frequency-windowing thus also affects the lower eigenvalues.

3) *Results Using Combined Frequency- and Time-Windowing*: Finally, we combined frequency- and time-windowing, as described in Algorithm 2. The results are shown in the bottom of Fig. 4. We observe that the eigenvalues from combined frequency- and time-windowed signals are very similar to those from the only frequency-windowed signals. It thus seems that the time-windowing does not incur a significant additional error on top of the inaccuracies that the frequency-windowing is incurring.

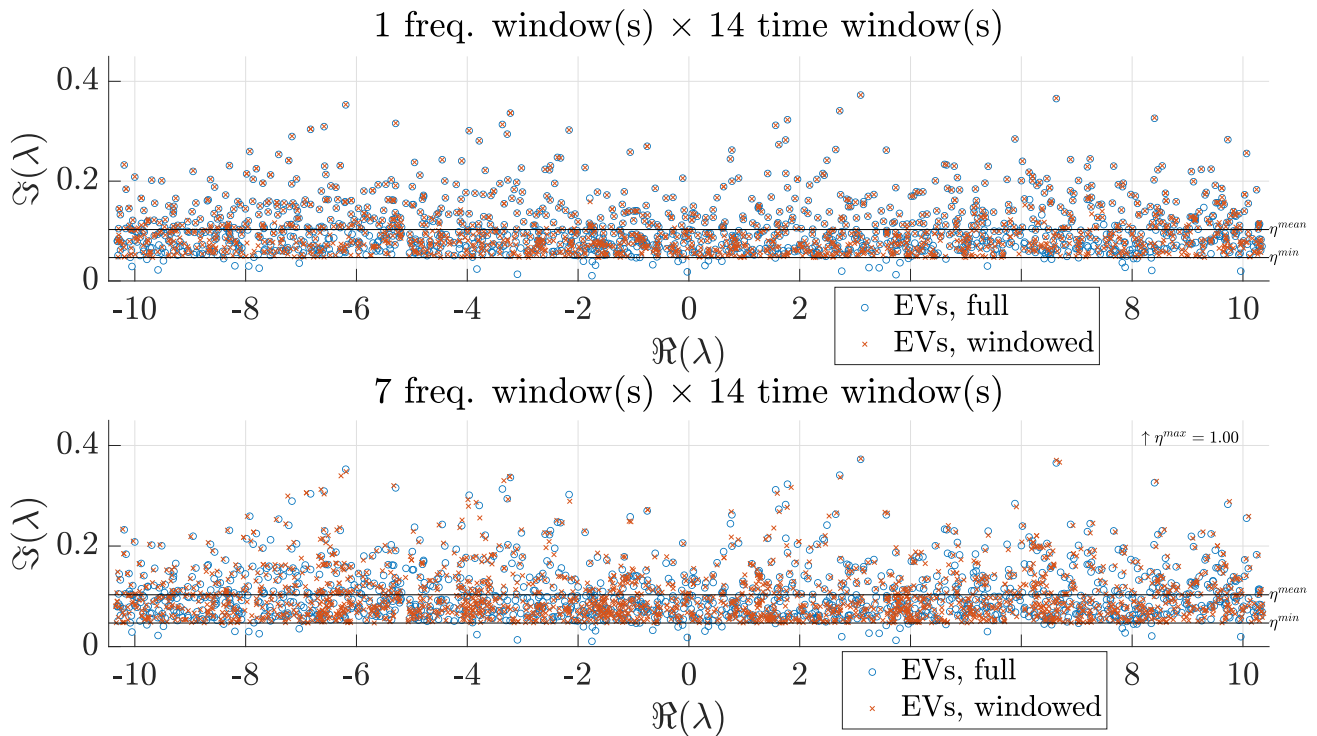


Fig. 5. Eigenvalues of a signal with 15,000 samples (at oversampling  $s = 3$ ), detected from windowed signals, and the higher eigenvalues detected from the full signal by Newton refining a dense grid of initial guesses. For both the top and bottom case, we used five time-windows. However, the top case used only one frequency-window (i.e., the full bandwidth), whereas the lower figure used seven frequency-windows.

In conclusion, the combined frequency- and time-windowing method yields quite accurate estimates with less than 2% error for the higher eigenvalues for the chosen example. Most of the error was caused by the frequency-windowing, while the time-windowing did not cause a visible error at all in the higher detected eigenvalues above  $\eta^{\text{mean}}$ .

In conclusion, we observe that time-windowing hardly infers any loss in accuracy, and may thus be used to speed up the calculation of the higher solitons. Furthermore, if a slight loss of accuracy in the eigenvalues is acceptable, the combined frequency- and time-windowing NFT can be used to obtain an even greater speed-up.

### B. Results for a Random 15,000 Sample Signal

After considering the 3000 sample signal, we are interested how the windowing algorithm performs for signals with very large time-bandwidth products. We therefore consider a signal with an occupied frequency-time domain five times as large as the 3000 sample signal, resulting in a signal of 15,000 samples. This long signal again consists of ideally low-pass filtered, complex, circularly symmetric, white Gaussian noise with zero mean, sampled at oversampling rate  $s = 3$  with respect to the Nyquist frequency corresponding to the occupied signal bandwidth. The time domain of this signal was  $T = [-375, 375]$ , sample time  $\Delta t = 0.05$ , and occupied bandwidth  $\Omega = [-20\pi/3, +20\pi/3] = [-20.9, 20.9]$ . The signal amplitude was scaled such that the mean energy density

corresponded to  $\eta^{\text{mean}} = 0.1$ , equal to the 3000 sample signal. The mean eigenvalue height of the 15,000 sample signal should therefore be equal to the 3000 sample signal, only approximately five times as many solitons should be present.

The 15,000 sample signal was too long to directly compute the eigenvalues with the used version of *FNFT*, as only spurious eigenvalues were detected that were far too high or far too low. We believe this is due to the rational approximation of the function  $a(\lambda)$ , which requires high precision arithmetic at some point for signals with very long durations. To obtain a ground truth, we instead used conventional Newton refinement to refine a dense grid of initial guesses. To verify that the found eigenvalues were indeed correct, the refinement was repeated using high-precision arithmetic.

We performed the combined frequency- and time-windowing NFT algorithm by running Algorithm 1 and then Algorithm 2 on the 15,000 sample signal, with the suggested parameters  $c_T = 4$ ,  $c_\Omega = 16$ ,  $R = 0.5$  and  $\varepsilon = 0.05$ . This resulted in  $N_\Omega = 7$  frequency-windows and  $M_T = 14$  time-windows.

The eigenvalues from the windowed signals are compared to the correct eigenvalues in Fig. 5. The top figure shows the result of only time-windowing, and the bottom of combined frequency- and time-windowing. When using only frequency-windowing, all detected eigenvalues were spurious. Even when we used 28 narrow frequency-windows (instead of 7) all eigenvalues were still spurious. This is likely again due to the rational approximation of  $a(\lambda)$ , that yields numerical issues for signals with long durations.

TABLE I

THE COMPUTATION TIMES FOR THE FULL NFT AND WINDOWING NFT OF VARIOUS SIGNALS (THE RESULTING EIGENVALUES WERE NOT VALIDATED). ALL SIGNALS WERE GENERATED AS BANDWIDTH-LIMITED WHITE NOISE SIGNALS, WITH APPROXIMATE MEAN ENERGY DENSITY CORRESPONDING TO  $\eta^{\text{mean}} = 0.1$ . ALL SIGNALS HAD THE SAME OVERSAMPLING RATE OF  $s = 3$

Full domain size ( $\Omega \times T$ )	Window size ( $\Omega^{\text{window}} \times T^{\text{window}}$ )	Number of samples, total / per window	Number of windows ( $N_{\Omega} \times M_T$ )	Full NFT computation time	windowing NFT computation time, all windows / single window
20.9 rad $\times$ 300	20.9 rad $\times$ 101	3000 / 1010	5 (1 $\times$ 5)	26.1 s	9.61 s / 3.20 s
20.9 rad $\times$ 300	11.3 rad $\times$ 300	3000 / 1626	3 (3 $\times$ 1)	26.1 s	22.0 s / 7.32 s
20.9 rad $\times$ 300	11.3 rad $\times$ 101	3000 / 547	15 (3 $\times$ 5)	26.1 s	7.84 s / 0.53 s
20.9 rad $\times$ 600	11.4 rad $\times$ 101	6000 / 547	33 (3 $\times$ 11)	122 s	17.7 s / 0.54 s
41.9 rad $\times$ 300	11.4 rad $\times$ 101	6000 / 547	35 (7 $\times$ 5)	85 s	19.1 s / 0.54 s
41.9 rad $\times$ 450	11.3 rad $\times$ 101	9000 / 546	56 (7 $\times$ 8)	224 s	26.6 s / 0.48 s
41.9 rad $\times$ 600	11.3 rad $\times$ 101	12000 / 546	77 (7 $\times$ 11)	442 s	37.9 s / 0.49 s
41.9 rad $\times$ 750	41.9 rad $\times$ 103	15000 / 2052	14 (1 $\times$ 14)	623 s	111 s / 7.92 s
41.9 rad $\times$ 750	11.1 rad $\times$ 103	15000 / 546	98 (7 $\times$ 14)	623 s	44.7 s / 0.46 s

We observe that time-windowing yields very accurate results for the majority of the eigenvalues above  $\eta^{\text{mean}}$ , while only a few of the high eigenvalues are visually different from the correct eigenvalues. A few eigenvalues are still missing (one example is around  $\lambda = 9.2 + 0.16i$ ), despite the extension of the acceptance region with  $\varepsilon = 0.05$ . We attempted to further enlarge the acceptance regions, but this resulted in several spurious eigenvalues being accepted, while still not capturing all missing eigenvalues. Apparently, a small number of high eigenvalues are still missed altogether. However, this issue could be overcome by redoing the calculation with an upsampled version of the signal (e.g., using band-limited interpolation). Upon upsampling the signal to  $s = 4.5$  (from  $s = 3$ , i.e. 50% more samples) and increasing the acceptance region to  $\varepsilon = 0.10$ , all missing eigenvalues above  $\eta^{\text{mean}}$  were recovered, although several poorer copies of eigenvalues with errors up to 5% were also accepted (figure omitted).

The results of the combined frequency- and time-windowing NFT are shown in the bottom of Fig. 5. We observe clear visual differences between the eigenvalues from the frequency- and time-windowed signals and the eigenvalues from the full signal. As for the 3000 sample signal, this is mostly the results of the frequency-windowing. Although some eigenvalues show an error of up to 10%, most eigenvalues are still within 1% of the correct value. The resulting eigenvalues are therefore still useful as rough estimates of the eigenvalues. They may also be used as initial points for local refinement using the full signal to find the correct eigenvalues.

In summary, we observe from the random 15,000 sample signal that time-windowing provides highly accurate results for the higher eigenvalues. Only frequency-windowing did not suffice to analyze the signal due to failures of the used NFT method. Finally, combined frequency- and time-windowing causes significant errors due to the frequency-windowing. We thus suggest to apply time-windowing to reduce the computation time for finding the higher eigenvalues, and only additionally use frequency-windowing when time-windowing alone does not provide sufficient speed up, or when a rough estimate of the discrete spectrum is sufficient.

### C. Speed up Due to Windowing

In this section, we consider the speed-up achieved through frequency- and/or time-windowing. Note that the time-bandwidth product of the window in (13) only depends on

the choice for the frequency- and time-broadening factors  $c_{\Omega}$  and  $c_T$ , but not on the signal itself. Independent of the occupied time-bandwidth product of the full signal, we may thus window the full signal into pieces with small and constant time-bandwidth product. The complexity of computing the NFT for each window is therefore approximately constant. As the time-bandwidth product per window is constant, the number of required windows increases linearly with the time-bandwidth product of the full signal. Therefore, a windowing NFT only requires  $\mathcal{O}(N)$  FLOPs, as opposed to a full NFT, which typically requires  $\mathcal{O}(N^2)$  or  $\mathcal{O}(KN)$  (with  $K$  the total number of solitons) for the considered configuration.

To demonstrate the speed-up, we considered a variety of low-pass filtered Gaussian white noise signals, with various bandwidths and durations. All signals were generated to have a mean energy density of approximately 0.026 1/rad, corresponding to  $\eta^{\text{mean}} = 0.1$ , and had oversampling rate of  $s = 3$ . For all signals we used *FNFT* to calculate the high eigenvalues from the full signal directly, and using the windowing NFT method with the suggested parameters. The correctness of the detected eigenvalues was not validated, only the computation times were recorded for the speed analysis.

The computation times are shown in Table I. The first three rows show the computation times of the 3000-sample signal when applying only frequency-windowing, only time-windowing, and combined frequency- and time-windowing NFT. Between rows 3-8, we gradually increased the number of samples in the signal, mostly by increasing the duration of the signal. We doubled the bandwidth of the signal for the signals of 6000 samples and longer, but we observe that this only affects the configuration of the windowing, while the computation time required for the windowing NFT hardly changes. We observe that the windowing NFT determines the higher eigenvalues faster than the full NFT in all considered cases, although the speed-up is most apparent for the longest signal of 15,000 samples, where a speed-up of  $\frac{623 \text{ s}}{44.7 \text{ s}} \approx 14$  times was observed for combined frequency- and time-windowing, and a speed-up of  $\frac{623 \text{ s}}{111 \text{ s}} \approx 6$  for only time-windowing. We observe that the full NFT indeed requires  $\mathcal{O}(N^2)$  computation time (e.g.,  $\frac{15000}{3000} = 5$  times more samples results in about  $\frac{623 \text{ s}}{26.1 \text{ s}} \approx 25$  times the computation time), while the windowing NFT only requires  $\mathcal{O}(N)$  time (e.g.:  $\frac{15000}{3000} = 5$  times more samples results in about  $\frac{44.7}{9.61} \approx 5$  times the computation time).

We thus conclude that the windowing NFT is much faster than the full NFT for signals with large time-bandwidth products. While the demonstrated window size works well in most applications, the windows size can be further shrunk to allow faster computations, or increased for higher accuracy of the eigenvalues.

## VI. CONCLUSION

We have proposed and validated a method to compute the significantly large solitonic components in the discrete part of the nonlinear Fourier transform for the nonlinear Schrödinger equation quickly and accurately, by partitioning the signal in the frequency and time domain. We divide the full occupied frequency-time domain into smaller overlapping windows, determine the higher eigenvalues within each individual window, reject the unreliable eigenvalues, and finally combine all accepted higher eigenvalues to obtain the full spectrum of higher eigenvalues associated with the larger solitons. The computation time of the NFT of a signal scales superlinearly in the occupied time-bandwidth product, so it is thus computationally faster to divide the full signal in many small frequency-time domains than to compute the NFT of the full signal. Our proposed frequency- and time-partitioning NFT uses a pre-defined time-bandwidth product for the windows, and thus only scales linearly in the number of used windows. It can therefore also be applied to very complicated signals for which other methods either fail or require very long computation times.

We tested the accuracy of the method on several signals and configurations, first by partitioning only the time domain, then by partitioning only the frequency domain, and finally by partitioning both the frequency and time domain. When only partitioning the time domain, the results are very good, and the higher solitons are captured with high accuracy. Only partitioning the frequency domain resulted in some loss of accuracy of the higher eigenvalues. Combined frequency- and time-partitioning resulted in the fastest result, but with a small loss in accuracy, mostly due to the frequency-partitioning.

To the best of our knowledge, we have thus presented the first method that can calculate the higher eigenvalues of signals with arbitrarily large time-bandwidth product, while the computation time depends only linearly on the occupied time-bandwidth product.

## REFERENCES

- [1] G. P. Agrawal, *Fiber-Optic Communication Systems*. Hoboken, NJ, USA: Wiley, 2012, vol. 222.
- [2] A. C. Scott, F. Chu, and D. W. McLaughlin, "The soliton: A new concept in applied science," *Proc. IEEE*, vol. 61, no. 10, pp. 1443–1483, Oct. 1973.
- [3] F. Mitschke, C. Mahnke, and A. Hause, "Soliton content of fiber-optic light pulses," *Appl. Sci.*, vol. 7, no. 6, 2017, Art. no. 635.
- [4] V. Zakharov and A. Shabat, "Exact theory of two-dimensional self-focusing and one-dimensional self-modulation of waves in nonlinear media," *Sov. Phys. JETP*, vol. 34, no. 1, 1972, Art. no. 62.
- [5] M. J. Ablowitz, D. J. Kaup, A. C. Newell, and H. Segur, "The inverse scattering transform-Fourier analysis for nonlinear problems," *Stud. Appl. Math.*, vol. 53, no. 4, pp. 249–315, 1974.
- [6] M. I. Yousefi and F. R. Kschischang, "Information transmission using the nonlinear Fourier transform, Part I: Mathematical tools," *IEEE Trans. Inf. Theory*, vol. 60, no. 7, pp. 4312–4328, Jul. 2014.
- [7] M. I. Yousefi and F. R. Kschischang, "Information transmission using the nonlinear Fourier transform, Part III: Spectrum modulation," *IEEE Trans. Inf. Theory*, vol. 60, no. 7, pp. 4346–4369, Jul. 2014.
- [8] Z. Dong et al., "Nonlinear frequency division multiplexed transmissions based on NFT," *IEEE Photon. Technol. Lett.*, vol. 27, no. 15, pp. 1621–1623, Aug. 2015.
- [9] H. Buelow, V. Aref, and W. Idler, "Transmission of waveforms determined by 7 eigenvalues with PSK-modulated spectral amplitudes," in *Proc. ECOC; 42nd Eur. Conf. Opt. Commun. VDE*, 2016, pp. 1–3.
- [10] S. T. Le, V. Aref, and H. Buelow, "Nonlinear signal multiplexing for communication beyond the Kerr nonlinearity limit," *Nature Photon.*, vol. 11, no. 9, pp. 570–576, 2017.
- [11] S. K. Turitsyn et al., "Nonlinear Fourier transform for optical data processing and transmission: Advances and perspectives," *Optica*, vol. 4, no. 3, pp. 307–322, 2017.
- [12] V. Aref, S. T. Le, and H. Buelow, "Modulation over nonlinear Fourier spectrum: Continuous and discrete spectrum," *J. Lightw. Technol.*, vol. 36, no. 6, pp. 1289–1295, Mar. 2018.
- [13] J. Koch, R. Weixer, and S. Pachnicke, "Equalization of soliton transmission based on nonlinear Fourier transform using neural networks," in *Proc. 45th Eur. Conf. Opt. Commun.*, 2019, pp. 1–4.
- [14] G. Zhou, T. Gui, C. Lu, A. P. T. Lau, and P.-K. A. Wai, "Improving soliton transmission systems through soliton interactions," *J. Lightw. Technol.*, vol. 38, no. 14, pp. 3563–3572, Jul. 2020.
- [15] G. Zhou, L. Sun, C. Lu, and A. P. T. Lau, "Multi-symbol digital signal processing techniques for discrete eigenvalue transmissions based on nonlinear Fourier transform," *J. Lightw. Technol.*, vol. 39, no. 17, pp. 5459–5467, Sep. 2021.
- [16] S. Wahls, "Shortening solitons for fiber-optic transmission," in *Proc. 17th Int. Symp. Wireless Commun. Syst.*, 2021, pp. 1–6.
- [17] P. de Koster and S. Wahls, "Dispersion and nonlinearity identification for single-mode fibers using the nonlinear Fourier transform," *J. Lightw. Technol.*, vol. 38, no. 12, pp. 3252–3260, Jun. 2020.
- [18] P. de Koster, J. Koch, O. Schulz, S. Pachnicke, and S. Wahls, "Experimental validation of nonlinear Fourier transform-based Kerr-nonlinearity identification over a 1600 km SSMF link," in *Proc. Opt. Fiber Commun. Conf.*, 2022, Paper W2A.39.
- [19] S. Sugavanam, M. K. Kopae, J. Peng, J. E. Prilepsky, and S. K. Turitsyn, "Analysis of laser radiation using the nonlinear Fourier transform," *Nature Commun.*, vol. 10, no. 1, pp. 1–10, 2019.
- [20] Y. Wang et al., "Soliton distillation of pulses from a fiber laser," *J. Lightw. Technol.*, vol. 39, no. 8, pp. 2542–2546, Apr. 2021.
- [21] Y. Wang et al., "Nonlinear Fourier transform enabled eigenvalue spectrum investigation for fiber laser radiation," *Photon. Res.*, vol. 9, no. 8, pp. 1531–1539, 2021.
- [22] F. Chen et al., "Characterization of sidebands in fiber lasers based on nonlinear Fourier transformation," *Opt. Exp.*, vol. 31, no. 5, pp. 7554–7563, 2023.
- [23] S. K. Turitsyn, I. S. Chekhovskoy, and M. P. Fedoruk, "Nonlinear Fourier transform for characterization of the coherent structures in optical microresonators," *Opt. Lett.*, vol. 45, no. 11, pp. 3059–3062, 2020.
- [24] J. Pan, T. Huang, Y. Wang, Z. Wu, J. Zhang, and L. Zhao, "Numerical investigations of cavity-soliton distillation in Kerr resonators using the nonlinear Fourier transform," *Phys. Rev. A*, vol. 104, no. 4, 2021, Art. no. 043507.
- [25] S. Turitsyn, I. Chekhovskoy, and M. Fedoruk, "Nonlinear Fourier transform for analysis of optical spectral combs," *Phys. Rev. E*, vol. 103, no. 2, 2021, Art. no. L020202.
- [26] S. K. Turitsyn, E. Sedov, A. Redyuk, and M. P. Fedoruk, "Nonlinear spectrum of conventional OFDM and WDM return-to-zero signals in nonlinear channel," *J. Lightw. Technol.*, vol. 38, no. 2, pp. 352–358, Jan. 2020.
- [27] G. Boffetta and A. R. Osborne, "Computation of the direct scattering transform for the nonlinear Schrödinger equation," *J. Comput. Phys.*, vol. 102, no. 2, pp. 252–264, 1992.
- [28] M. I. Yousefi and F. R. Kschischang, "Information transmission using the nonlinear Fourier transform, Part II: Numerical methods," *IEEE Trans. Inf. Theory*, vol. 60, no. 7, pp. 4329–4345, Jul. 2014.
- [29] A. Vasylichenkova, J. E. Prilepsky, D. Shepelsky, and A. Chattopadhyay, "Direct nonlinear Fourier transform algorithms for the computation of solitonic spectra in focusing nonlinear Schrödinger equation," *Commun. Nonlinear Sci. Numer. Simul.*, vol. 68, pp. 347–371, 2019.

- [30] S. Chimmalgi, P. J. Prins, and S. Wahls, "Fast nonlinear Fourier transform algorithms using higher order exponential integrators," *IEEE Access*, vol. 7, pp. 145161–145176, 2019.
- [31] J. He et al., "Adaptive trust-region-based algorithm for the discrete eigenvalue evaluation of the direct nonlinear Fourier transform," *Opt. Lett.*, vol. 47, no. 16, pp. 4195–4198, 2022.
- [32] S. Wahls and H. V. Poor, "Introducing the fast nonlinear Fourier transform," in *Proc. IEEE Int. Conf. Acoust., Speech Signal Process.*, 2013, pp. 5780–5784.
- [33] A. Vasylenkova, J. E. Prilepsky, and S. K. Turitsyn, "Contour integrals for numerical computation of discrete eigenvalues in the Zakharov–Shabat problem," *Opt. Lett.*, vol. 43, no. 15, pp. 3690–3693, 2018.
- [34] E. V. Sedov, I. S. Chekhovskoy, J. E. Prilepsky, and M. P. Fedoruk, "Application of neural networks to determine the discrete spectrum of the direct Zakharov–Shabat problem," *Quantum Electron.*, vol. 50, no. 12, 2020, Art. no. 1105.
- [35] I. Chekhovskoy, S. B. Medvedev, I. Vaseva, E. Sedov, and M. P. Fedoruk, "Introducing phase jump tracking—a fast method for eigenvalue evaluation of the direct Zakharov–Shabat problem," *Commun. Nonlinear Sci. Numer. Simul.*, vol. 96, 2021, Art. no. 105718.
- [36] V. Aref, S. T. Le, and H. Buelow, "An efficient nonlinear Fourier transform algorithm for detection of eigenvalues from continuous spectrum," in *Proc. Opt. Fiber Commun. Conf.*, Optica Publishing Group, 2019, Paper M11–5.
- [37] S. Hari, M. I. Yousefi, and F. R. Kschischang, "Multieigenvalue communication," *J. Lightw. Technol.*, vol. 34, no. 13, pp. 3110–3117, Jul. 2016.
- [38] J. Koch, K. Chan, C. G. Schaeffer, and S. Pachnicke, "Signal processing techniques for optical transmission based on eigenvalue communication," *IEEE J. Sel. Topics Quantum Electron.*, vol. 27, no. 3, May/Jun. 2021, Art. no. 5100214.
- [39] R. Zhang et al., "Optimal design of eigenvalues for the full-spectrum modulated nonlinear frequency division multiplexing transmission system," *IEEE Photon. J.*, no. 3, Jun. 2023, Art. no. 7200908.
- [40] G. Roberti, G. El, A. Tovbis, F. Copie, P. Suret, and S. Randoux, "Numerical spectral synthesis of breather gas for the focusing nonlinear Schrödinger equation," *Phys. Rev. E*, vol. 103, no. 4, 2021, Art. no. 042205.
- [41] P. Suret, M. Dufour, G. Roberti, G. El, F. Copie, and S. Randoux, "Soliton refraction through an optical soliton Gas," 2023, *arXiv:2303.13421*.
- [42] S. Randoux, P. Suret, and G. El, "Inverse scattering transform analysis of rogue waves using local periodization procedure," *Sci. Rep.*, vol. 6, no. 1, pp. 1–11, 2016.
- [43] A. R. Osborne, M. Onorato, and M. Serio, "The nonlinear dynamics of rogue waves and holes in deep-water gravity wave trains," *Phys. Lett. A*, vol. 275, no. 5/6, pp. 386–393, 2000.
- [44] A. Slunyaev, "Analysis of the nonlinear spectrum of intense sea wave with the purpose of extreme wave prediction," *Radiophysics Quantum Electron.*, vol. 61, no. 1, pp. 1–21, 2018.
- [45] M. Onorato et al., "Observation of a giant nonlinear wave-packet on the surface of the ocean," *Sci. Rep.*, vol. 11, no. 1, 2021, Art. no. 23606.
- [46] J. Koch, S. Li, and S. Pachnicke, "Transmission of higher order solitons created by optical multiplexing," *J. Lightw. Technol.*, vol. 37, no. 3, pp. 933–941, Feb. 2019.
- [47] A. Hasegawa and Y. Kodama, *Solitons in Optical Communications*. Oxford, U.K.: Oxford Univ. Press, 1995.
- [48] L. M. Alonso, "Effect of the radiation component on soliton motion," *Phys. Rev. D*, vol. 32, no. 6, 1985, Art. no. 1459.
- [49] M. Borghese, R. Jenkins, and K. D.-R. McLaughlin, "Long time asymptotic behavior of the focusing nonlinear Schrödinger equation," *Annales de l'Institut Henri Poincaré C, Analyse non linéaire*, vol. 35, pp. 887–920, 2018.
- [50] S. Medvedev, I. Vaseva, I. Chekhovskoy, and M. Fedoruk, "Exponential fourth order schemes for direct Zakharov–Shabat problem," *Opt. Exp.*, vol. 28, no. 1, pp. 20–39, 2020.
- [51] P. J. Prins and S. Wahls, "Soliton phase shift calculation for the Korteweg–de Vries equation," *IEEE Access*, vol. 7, pp. 122914–122930, 2019.
- [52] S. Chimmalgi and S. Wahls, "Bounds on the transmit power of b-modulated NFD systems in anomalous dispersion fiber," *Entropy*, vol. 22, no. 6, 2020, Art. no. 639.
- [53] S. Wahls, S. Chimmalgi, and P. J. Prins, "FNFT: A software library for computing nonlinear Fourier transforms," *J. Open Source Softw.*, vol. 3, no. 23, 2018, Art. no. 597.